Modeling Li-Ion Battery Temperature and Expansion Force during the Early Stages of Thermal Runaway Triggered by Internal Shorts

Ting Cai, [z] **Anna G. Stefanopoulou,*** **and Jason B. Siegel** [*]

Department of Mechanical Engineering, University of Michigan, Ann Arbor, Michigan, USA

Thermal runaway of Li-ion batteries is a major safety issue. It is a complex process involving high heat generation, fast temperature rise and significant amounts of generated gas. Modeling thermal runaway will enable a better understanding and earlier detection of the phenomenon. Since the majority of the thermal runaway incidents are triggered by an internal short circuit, this paper presents a model describing lithium-ion battery thermal runaway triggered by an internal short. In this study, two internal short circuit experiments were conducted on two nickel manganese cobalt oxide pouch cells, one that was fully charged and one half charged. The fully charged cell went into a quick thermal runaway, while the half-charged cell evolved only into a slow, self-discharge process. Both of these experiments demonstrate that a huge battery swelling force signal can be detected prior to the surface temperature rise during an internal short circuit event. This thermal runaway model is the first attempt to connect gas generation with force signal, and successfully capture the early stages of thermal runaway, including the early rise of force signal, after parameter tuning. This model's use of force measurement enables higher confidence in the early detection of thermal runaway induced by an internal short.
 [DOI: 10.1149/2.1561910jes]

Manuscript submitted October 12, 2018; revised manuscript received May 31, 2019. Published July 8, 2019.

Lithium ion batteries are widely used in energy storage and offer significant improvements in electric vehicles. However, the growth in battery energy density increases the risk and severity of battery failures. With the increasing numbers of electric vehicles and consumer electronics applications of large capacity Li-ion batteries, battery fires and explosions accidents are increasing worldwide. Many of these accidents start with an overcharge, over-discharge, or a battery separator penetration due to mechanical abuse[1] that lead to battery temperature elevation, self-heating and finally thermal runaway (TR). In many cases, this process begins with an internal short circuit (ISC) that causes self-heating and can elevate the battery temperature above 130°C. This, in turn, can result in side reactions including a breakdown of the Solid Electrolyte Interface (SEI) layer.[2] These side reactions quickly produce additional heat and can lead to battery thermal runaway. Common hazards of battery thermal runaway include toxic off-gassing, smoke, fire, and even an explosion.[3]

To develop an early detection method, it is important to model the thermal runaway process. The proposed model divides the battery into three sections: core, middle layer, and surface layer,[4] and identifies the heat released per the electrochemical energy stored in each section. The model contains four sub-models: an electrical model for the internal short circuit process, a side reactions model for exothermic reactions of active materials, a thermal model for battery temperature and a gas evolution model to predict early gas generation.

Many researchers have made an effort toward a battery thermal model that explains battery temperature evolution. Hatchard[5] used a spatially discretized thermal model, with N concentric rings, to account for the radial temperature distribution of a battery during thermal runaway. This showed that there is very little difference in the onset temperature for thermal runaway (3°C) during oven testing, as compared to the lumped thermal mass approach. Furthermore, since the entire cell is at an elevated temperature when the exothermic process begins, the reaction progresses more uniformly along the radius of the cell. Coman[6] used lumped thermal models to describe battery temperature during thermal runaway. The lumped thermal model assumes a uniform temperature distribution and one temperature state to represent the whole cell. This assumption is valid for an 18650 cell, which has a small Biot number ($B_i = 0.051$),[6] and they showed the battery surface temperature from the model is very close to the experiment measurement. In the case of a local internal short circuit, however, the ohmic heat generation will be concentrated in a small localized area, causing a large spatial temperature gradient in a focused space. To address this inhomogeneity, others have used a finite element approach, with high computation cost and difficulty in tuning.[7,8] By using the proposed three-section thermal model, a reasonable trade-off can be achieved between computational complexity and accuracy.

In modeling the internal short, the resistance of the ISC is a critical parameter for determining the severity and time to onset of the TR event.[9] However, few papers address calculation of the short resistance depends on the area of the separator failure. Guo[10] explained the ISC caused by over-discharge and used experimental data to fit a curve of ISC resistance with over-discharge capacity. Coman[6] developed a model for energy released due to the ISC with an efficiency factor that was fitted to their experiment data. The fitting approach worked well with the specific cells in the experiment, but is difficult to be applied to varying Li-ion battery chemistries. This study presents an electrical model that describes ISC and proposes a finite element method for solving ISC resistance of the battery for small geometric areas.

Side reaction models are well established for major exothermic reactions during a TR event. Previous studies already provide robust reaction kinetic parameters measured from Accelerated Rate Calorimetry (ARC) experiments during thermal runaway.[5,11] Hatchard[5] developed these side reaction models for major exothermic side reactions including SEI decomposition, anode decomposition, and cathode decomposition. Kim[12] extended the model to include electrolyte decomposition, and these models have been used by many researchers over the years. Ren[13] developed a set of thermal runaway side reaction chemical kinetics based on DSC testing that includes six exothermic reactions in the model, SEI decomposition, anode-binder reaction, anode-electrolyte reaction, cathode-electrolyte reaction, cathode-binder reaction, and cathode decomposition.

During the early stage of thermal runaway, a significant amount of gas and electrolyte is vented to the outer regions of the battery.[14] Coman[15] studied and modeled this electrolyte and ejecta venting during thermal runaway. They showed how the amount of ejected material impacts the peak temperature of thermal runaway due to the Joule-Thomson effect during venting and removal of hot materials from the cell during the later stages of thermal runaway. Previous experimental studies for commercial 18650 Li-ion batteries from Lammer et al.[16] on the composition of vented gas showed that most of the gas is CO_2 during the first gas venting event. Other studies have demonstrated that SEI decomposition is the primary source of CO_2 generation during the early stages of thermal runaway.[1] Pannala[17] characterized a battery swelling and the immediate rise of force signal during a pouch cell thermal runaway event, and hot gases were detected after the force

*Electrochemical Society Member.
[z]E-mail: tingcai@umich.edu

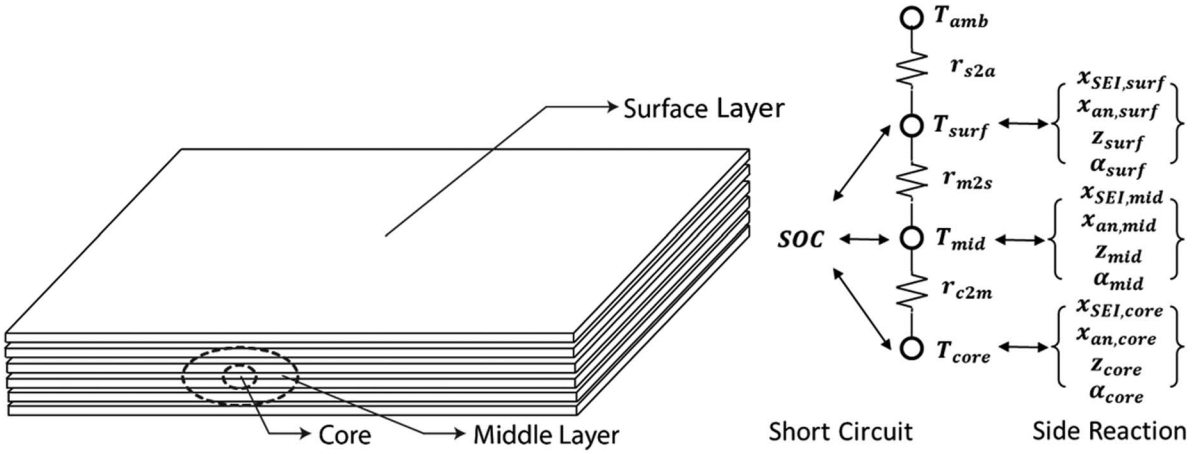

Figure 1. Three Section Model with Battery Discretized into Core, Middle Layer and Surface Layer.

drops. Based on these results, our study assumes that gas from SEI decomposition is the most significant contributor to battery swelling and force signal rise during the first few seconds following an ISC event. This study is the first attempt to make a connection between side reactions and force of battery swelling for modeling purposes.

To tune the model, two experiments were conducted with 4.5 Ah pouch cells for which an ISC was triggered at 57°C with different initial State of Charge (SOC). In a previous study, the battery internal short circuit was emulated by triggering a shape memory alloy to penetrate the separator.[18] Here we used a wax-based melt device in the separator to trigger the internal short[19] for model validation. In our experiments, we demonstrated two modes for the ISC event. The cell with 50% SOC didn't trigger thermal runaway, while the cell with 100% SOC went into a quick thermal runaway. The model fits well for temperature and force signal on both experiments, by capturing the surface temperature rise and gas volume change inside the cell compared with force measurement. The model and experiments with the early rise of force signal show the potential of using the mechanical behavior as an early indicator for ISC induced thermal runaway. The model developed here is not predictive, and can only capture the observed experimental results after parameter tuning. Future work is needed to validate and enable the predictive ability of this model.

The major contributions of this paper are:

- Three section discretization is proposed and parameterized to capture the high rate of core temperature change and the peak temperature; while at the same time, matching the surface temperature with the measurements. The prior work on TR modeling either employed a fine mesh using the Finite Element Method[8] or used a single bulk temperature state.[6] The model presented here represents a trade-off between computational complexity and accuracy and is useful for online model-based fault detection.
- Detailed modeling work is developed on ISC resistance as a function of its spatial area. The model also couples cell SOC with the anode decomposition process. Since multiple reactions compete for available lithium at the negative electrode, including the impact of self-discharge caused by the ISC on SOC is crucial for predicting TR. With these improvements, the proposed model can better evaluate the peak temperature and SOC change during an ISC event which triggers TR.
- Two experiments are shown for two different SOC levels with a triggering ISC. The cell with high SOC led to a quick thermal runaway, and the other cell with low SOC led to a slow self-discharge after triggering ISC. The model can capture both phenomena after proper parameter tuning, including the type of ISC mode in the event.
- Matching the model and experiments with the force signal show the potential of using the mechanical behavior as an early indication for ISC-induced thermal runaway.

Thermal Runaway Model

The battery's internal temperature states are divided to three sections, and the mass of each section is scaled proportionally to its volume fraction. This uneven coarse discretization better captures the relatively small area adjacent to the internal short circuit which heats more rapidly than the surrounding volume. The remainder of the cell mass, which lags in heating, contains the bulk of the cell material. As Fig. 1 illustrates, the overall thermal runaway model includes a three-state thermal model, a side reaction model which tracks the consumption of active materials, and an electrical equivalent circuit model. The model has three temperature states, four side reaction states in each section, and one state for the cell state of charge according to an electrical equivalent circuit model. In total, the three-section model consists of 16 states. The nomenclature can be found in the appendix.

Three-state thermal model.—For thermal runaway triggered by ISC, the ISC area has a significant volumetric heat rate and will have a relatively fast temperature rise compared to the surface of the cell. To address this inhomogeneity of temperature within the battery, we need to discretize the battery into several sections. We found that three sections for temperature discretization achieved good accuracy while at the same time maintained reasonable computational complexity.

A three-state thermal model describes battery core temperature (T_c), middle layer temperature (T_m), and surface layer temperature (T_s). The battery core represents the area in which the ISC first occurs. In Figure 1, this location is schematically shown at the center of the cell. However, it need not necessarily be located at the geometric center. The proposed model also applies to cases where the ISC is located near the surface, as shown later in the experimental results. It is the relative volumes rather than the specific ISC location, that is critical for capturing the temperature rise during thermal runaway. Specifically, the dynamic evolution of the core temperature state is

$$C_p m_{core} \frac{dT_{core}}{dt} = (\dot{Q}_{exo,core} + \dot{Q}_{ohmic,core}) + \frac{T_{mid} - T_{core}}{r_{c2m}} \quad [1]$$

where T_{core} and T_{mid} represent the core and middle layer temperatures respectively and r_{c2m} is the thermal resistance between the core and middle layer. Similarly the middle and surface layer temperatures are given by

$$C_p m_{mid} \frac{dT_{mid}}{dt} = (\dot{Q}_{exo,mid} + \dot{Q}_{ohmic,mid}) - \frac{T_{mid} - T_{core}}{r_{c2m}} + \frac{T_{surf} - T_{mid}}{r_{m2s}} \quad [2]$$

$$C_p m_{surf} \frac{dT_{surf}}{dt} = (\dot{Q}_{exo,surf} + \dot{Q}_{ohmic,surf}) + \frac{T_{amb} - T_{surf}}{r_{s2a}} - \frac{T_{surf} - T_{mid}}{r_{m2s}} \quad [3]$$

The r_{c2m}, r_{m2s}, r_{s2a} terms are equivalent thermal resistance.

The battery core section refers to the battery area affected by initial ISC, and the m_{core} parameter can be derived if the ISC area is known. Theoretically, the mass ratio of each layer equals to the volume ratio of the each layer when assuming uniform density ($m_{core} = m_{cell}\frac{V_{core}}{V_{cell}}$, $m_{mid} = m_{cell}\frac{V_{mid}}{V_{cell}}$), where m_{cell} is the battery cell mass, and V_{core} and V_{mid} are the volumes of core and middle layer). In this study, for a cell with a wax-based separator, the core mass ideally can be calculated by the area of the wax part separator and the electrode sheet thickness. The volume of a cylindrical ISC area can be expressed as

$$V_{core} = \pi r_{short}^2 H \quad [4]$$

where r_{short} is the radius of the short circuit region, and H is the height of the cylindrical short area, which is the sum of two electrode sheets thickness and the separator thickness. However, the initial ISC also heats up regions outside of ISC area during the internal short circuit process, so the relative size of the volumes for three sections are tuned in this study. The correlation between the three section sizes and the ISC device volume will be explored in subsequent work with more available data.

The total heat generation by the side reactions is given by

$$\dot{Q}_{exo,*} = \dot{Q}_{an,*} + \dot{Q}_{ca,*} + \dot{Q}_{SEI,*} \quad [5]$$

where $*$ corresponds to the core, middle and surface layers. The total heat rate from all side reactions depends on the three exothermic decomposition reactions in each layer. These reactions drive the temperature rise, and the temperature rise will accelerate these reactions, leading to thermal runaway.

Electrical model.—During a thermal runaway event, besides exothermic side reactions that generate heat, the battery short circuit will also generate ohmic heat. The thermal and decomposition evolution depends on the rate of this ohmic heat generation and its dissipation rate to the surrounding material. This paper focuses on the internal short circuit that occurs in a small region of a battery and presents a model for its local heating. The battery terminal voltage can be represented by an equivalent circuit model

$$V_T = U(SOC) - I \cdot R_{cell} \quad [6]$$

where I is the discharge current, which is equal to the short current I_{short} when there is no load, as shown in Fig. 2a. The nominal cell internal resistance is R_{cell} and $U(SOC)$ is the battery open circuit voltage (OCV). The OCV is a function of SOC, as shown in Fig. 2b.

Rheinfeld[20] used the 1 kHz impedance as cell resistance to evaluate the theoretical maximum short circuit at the first few seconds of the internal short process. Here, 1 kHz impedance of the cell from EIS testing ($R_{1kHz} = 4.76m\Omega$) will be used to represent cell resistance for an modeling internal short circuit.

Equivalent circuit model for ISC.—From the ISC resistance, an equivalent circuit model can be developed to describe the internal short circuit process. Previous studies on ISC mechanisms have also used an equivalent circuit model with area dependent resistance.[10] In this study for a self-induced thermal runaway case, we assume no external wires connecting the positive and negative electrodes of the cell. The corresponding equivalent circuit model is shown in Fig. 2a. Therefore short circuit current can be found using Kirchoff's laws directly for the simple circuit.

$$I_{short} = \frac{U(SOC)}{R_{cell} + R_{short}} \quad [7]$$

The total heat release due to self discharge is given by,

$$\dot{Q}_{ohmic} = I_{short}^2 (R_{cell} + R_{short}) \quad [8]$$

To be noted, the ohmic heat $I^2 R_{short}$ is distributed only in the short circuit area, and the overall heat rate $I^2 R_{cell}$ is distributed among all cell. Specifically, when the ISC starts in the battery core, the ohmic heat will be distributed as following:

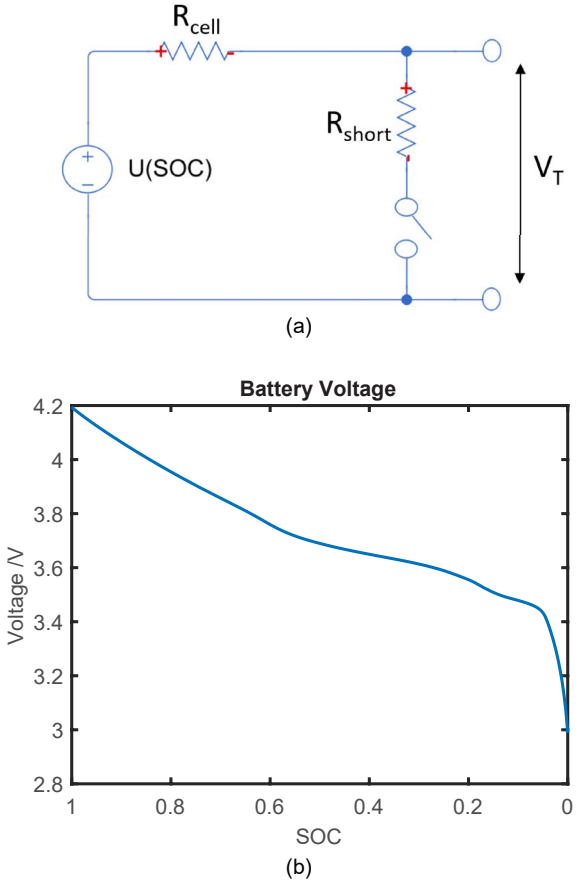

Figure 2. Electrical Model (a) Equivalent Circuit Model for ISC Electrical Model (b) Battery Open Circuit Voltage $U(SOC)$.

$$\dot{Q}_{ohmic,core} = I_{short}^2 R_{short} + \frac{m_{core}}{m_{cell}} I_{short}^2 R_{cell} \quad [9]$$

$$\dot{Q}_{ohmic,mid} = \frac{m_{mid}}{m_{cell}} I_{short}^2 R_{cell} \quad [10]$$

$$\dot{Q}_{ohmic,surf} = \frac{m_{surf}}{m_{cell}} I_{short}^2 R_{cell} \quad [11]$$

where the subscript core, mid, surf corresponds to the core, middle and surface layers of the battery respectively. Adjusting the resistance values can increase the heat rate in the short circuit area to be much higher than the rest of cell so that the short area will experience significant temperature rise before the rest of the cell.

ISC resistance.—Four major types of internal short circuits have been discussed in previous studies,[18] with Cathode to Anode ISC (or called Type A ISC) being the most common type of ISC. Typically the ISC area is small in comparison with the total cell area. In cathode to anode ISC, if the ISC area is caused by a penetrated separator and the cathode and anode is connected through high conductivity materials, such as iron, then the resistivity of the electrode's active material dominates the resistance of the short. A zero-th order approximation of true electric resistance can be derived using geometric resistance:

$$R_{geo} = \rho \frac{L}{S} \quad [12]$$

where ρ is electric resistivity, L is the length and S is the cross-sectional area for uniform resistive property material.

For small areas, however, the distribution of the potential field near the edge cannot be ignored. Thus, a Comsol simulation was developed for a unit current flowing through the ISC area. The simulation solves

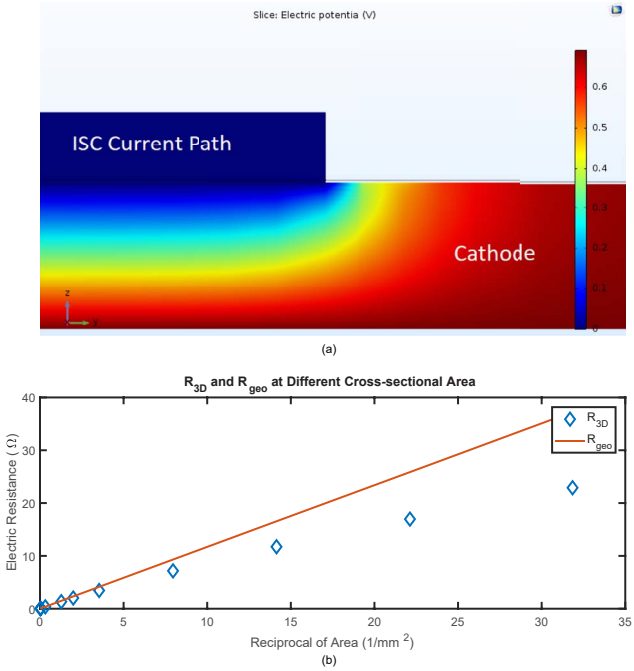

Figure 3. ISC Resistance Computation. (a) Electric Potential at Short Circuit Area (b) Comparison between R_{3D} and R_{geo}.

Ohm's law in 3D at a fixed applied current to compute the electric field:

$$\mathbf{E} = \rho \mathbf{J} \quad [13]$$

with $\mathbf{J}$ being the current density. Then R_{3D} is calculated numerically by:

$$R_{3D} = \frac{-\int \mathbf{E} \cdot d\mathbf{x}}{I} \quad [14]$$

where $d\mathbf{x}$ is the element of the path along electric field, and I is the total applied current, which equals to the integration of current density over the cross-sectional area ($I = \int \mathbf{J} dxdy$).

Figure 3a shows a 2-D slice of the electrical potential distribution of ISC current path at the short circuit area with a unit applied current. The ISC resistance is obtained numerically from this simulation for a range of areas. The ISC resistance is nearly inversely proportional to the ISC area, where a smaller ISC area will have larger short resistance. As Fig 3b indicates, geometric resistance estimates the ISC resistance well for large ISC areas. However, for small areas, the geometric resistance overestimates the ISC resistance where the edge effects are significant. Detailed results for the comparison of equivalent ISC resistance (R_{3D}) and geometric resistance (R_{geo}) are shown in Fig. 3a. Based on this result, R_{geo} is a good estimation of R_{3D} when the ISC resistance is lower than 5Ω. For ISC resistance greater than 5Ω the area dependence is non-linear, and the full 3D potential field should be evaluated as shown in Figure 3a, if the short area is known. In the following study, R_{3D} will be adopted for ISC resistance R_{short} greater than 5Ω based on the error shown in Figure 3a.

Temperature dependency for cell resistance.—As the cell temperature increases significantly during the thermal runaway process, the temperature dependency for electrical resistance needs to be taken into consideration. The diffusivity of ion transport increases exponentially with temperature.[21] The cell resistance is then assumed to decrease exponentially with battery core temperature rise, while the short circuit resistance is assumed constant with temperature change. Under this assumption, an exponential temperature dependency relation is selected from Lin[22] to represent the cell resistance:

$$R_{cell} = R_{e,ref} \exp\left(T_{ref}/T\right) \quad [15]$$

where $R_{e,ref}$ is the reference resistance value at a reference temperature T_{ref}. The exponential relationship is directly adopted from Lin,[22] while the reference resistance value is selected to reflect the measured 1 kHz impedance at 20°C. In this study, $R_{e,ref}$ is taken as $0.0246m\Omega$, and T_{ref} is taken as $1543K$.[22]

However, since the cell temperature is discretized in this model, so the cell resistance should be expressed as a function of three sections temperature. The cell resistance can be represented by the three sections, where the temperature dependency comes from the temperature of each section:

$$R_{cell} = \frac{1}{1/R_{cell,core} + 1/R_{cell,mid} + 1/R_{cell,surf}} \quad [16]$$

where $R_{cell,core}, R_{cell,mid}, R_{cell,surf}$ is the cell electrical resistance based on core, middle layer and surface layer. The temperature dependency for each of the electrical resistances can be expressed as:

$$R_{cell,*} = R_{*,ref} \exp\left(T_{ref}/T_*\right) \quad [17]$$

where $*$ corresponds to core, middle layer and surface layer. $R_{*,ref}$ is the reference resistance value for layer $*$, and is a function of mass ratio of layer $*$.

$$R_{*,ref} = \frac{R_{e,ref}}{m_*/m_{cell}} \quad [18]$$

where m_* is the mass of layer $*$, and $R_{e,ref}$ is the reference resistance value for the whole cell ($0.0246m\Omega$).

Additional assumptions for short circuit.—We assume that the core part structure collapses at the melting temperature of the current collector and will interrupt the short. We then assume that the internal short circuit at that high-temperature area will stop. Further, due to heat propagation, the neighboring area will trigger an internal short circuit once the separator in neighboring areas melts. For simplicity, we assume that the short circuit happens only at one place at a time and that the neighboring area develops an internal short after the previous section collapses.

Side reaction model.—To simplify the study, the side reaction model includes only three major side reactions, SEI decomposition, anode decomposition, and cathode decomposition.[5] The side reaction model used in this work is based on the work of Coman,[6] where the Arrhenius equations for the temperature dependent reaction rates of thermal runaway side reactions are included. To match the NMC cathode material used in our experiment, all side reaction parameters are adopted from Dong.[23] Most of the reaction parameters are the same as Coman,[6] although some parameters are different, including the heat release, activation energy, pre-exponential term of NMC cathode decomposition, and the pre-exponential term of SEI. Detailed values and sources for side reaction parameters are listed in Table II.

Solid electrolyte interface (SEI) decomposition.—The SEI starts to decompose first at temperatures above 130°C.[2]

$$\frac{dx_{SEI,*}}{dt} = -A_{SEI} \cdot x_{SEI,*} \cdot \exp\left(-\frac{E_{SEI}}{k_b T_*}\right) \quad [19]$$

where $x_{SEI,*}$ is the fraction of Li in the SEI in layer * ($* = core, mid, surf$), A_{SEI} is the frequency factor for SEI decomposition and E_{SEI} is the activation energy for SEI decomposition, k_b is Boltzmann's constant, and T_* is the temperature in layer *. The heat released by SEI decomposition in each layer * is given by:

$$\dot{Q}_{SEI,*} = -m_{an,*} \cdot h_{SEI} \cdot \frac{dx_{SEI,*}}{dt} \quad [20]$$

where h_{SEI} is the reaction enthalpy of SEI decomposition. The mass fraction of anode material in each layer is given by the total anode mass multiplied by the mass fraction of the layer to the cell total mass $m_{an,*} = m_{an} \cdot m_*/m_{cell}$.

Anode decomposition.—Intercalated lithium in graphite starts to react with the electrolyte at high temperature. This side reaction starts at around 180°C.[24]

$$\frac{dx_{an,*}}{dt} = -A_{an} \cdot x_{an,*} \cdot \exp\left(-\frac{E_{an}}{k_b T_*}\right) \cdot \exp\left(-\frac{z_*}{z_0}\right) \quad [21]$$

where $x_{an,*}$ is the fraction of Li in the anode in layer *, A_{an} is the frequency factor for anode decomposition and E_{an} is the activation energy for anode decomposition. In addition, the relative SEI thickness (z) is also considered in anode decomposition (tunneling effect[11]).

$$\frac{dz_*}{dt} = A_{an} \cdot x_{an,*} \cdot \exp\left(-\frac{E_{an}}{k_b T_*}\right) \cdot \exp\left(-\frac{z_*}{z_0}\right) \quad [22]$$

where z_* is a dimensionless number representing relative SEI thickness in layer *. The heat released by decomposition of the anode in each layer * is given by:

$$\dot{Q}_{an,*} = -m_{an,*} \cdot h_{an} \cdot \frac{dx_{an,*}}{dt} \quad [23]$$

where h_{an} is the reaction enthalpy of anode decomposition.

Cathode decomposition.—Finally at the highest temperature, the cathode material starts to decompose releasing oxygen and heat. For the NMC battery chemistry, this side reaction usually starts at 240°C.[25] The rate of conversion, of the cathode active material is given by:

$$\frac{d\alpha_*}{dt} = \alpha_*(1-\alpha_*) \cdot A_{ca} \cdot \exp\left(-\frac{E_{ca}}{k_b T_*}\right) \quad [24]$$

where α_* is the degree of conversion of cathode decomposition in layer $*$. The reaction stops when $\alpha_* = 1$ and all of the cathode material in that layer has been consumed. A_{ca} is the frequency factor for cathode decomposition and E_{ca} is the activation energy for cathode decomposition. The heat generation in each layer is proportional to the rate of conversion given by:

$$\dot{Q}_{ca,*} = m_{ca,*} \cdot h_{ca} \cdot \frac{d\alpha_*}{dt}. \quad [25]$$

where h_{ca} is the reaction enthalpy of cathode decomposition. Similarly to the anode, the mass fraction of cathode material in each layer is given by the total anode mass multiplied by the mass fraction of the layer to the cell total $m_{ca,*} = m_{ca} \cdot m_*/m_{cell}$.

Equations 19–25 describe the thermal runaway side reactions. The temperature in Eqs. 19–25 should be the local temperature (core, middle, surface layer). At different regions of the battery, we will see different reaction rates for the side reactions.

Coupling ISC and anode decomposition.—The anode decomposition and self-discharge due to ISC are coupled in this work, as they both consume Li in the anode. As shown in Figure 4, both processes cause SOC to decrease. The SOC is an important parameter in the side reaction model and the electrical model which impacts the total heat release. Higher initial SOC increases the chance of thermal runaway since the heat released during the ISC is larger. After coupling, SOC can be expressed as the weighted average fraction of Li of the anode in all layers ($x_{an,*}$).

$$SOC = \sum_* \frac{m_*}{m_{cell}} \frac{x_{an,*}}{x_{an,0}} \quad [26]$$

where $x_{an,0}$ is the initial Li fraction in an anode for fully charged cells. Then anode decomposition and SOC change of a cell with capacity C can be re-written as:

$$\frac{dSOC}{dt} = -\frac{I_{short}}{C} - \frac{1}{x_{an,0}} \sum_* \frac{m_*}{m_{cell}} A_{an} \cdot x_{an,*} \cdot \exp\left(-\frac{E_{an}}{k_b T_*}\right) \cdot \exp\left(-\frac{z_*}{z_0}\right) \quad [27]$$

where * here represents core, middle layer or surface layer, and $x_{an,*}$ represent local x_{an} in core, middle layer or surface layer. Assuming that

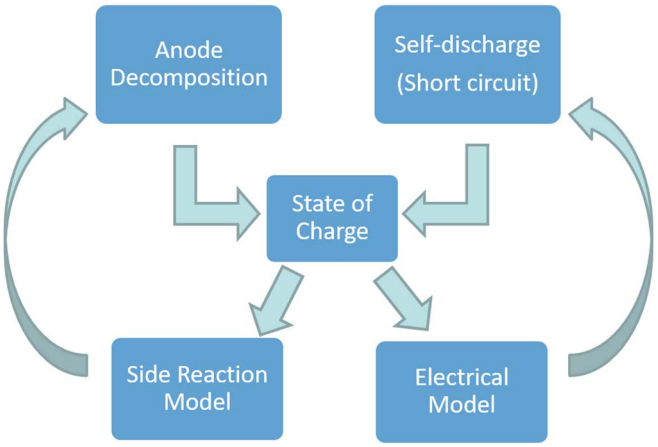

Figure 4. Coupling ISC and Anode Decomposition.

I_{short} depletes lithium in all sections proportionally, then the fraction of lithium in each section is computed by:

$$\frac{dx_{an,*}}{dt} = -A_{an} \cdot x_{an,*} \cdot \exp\left(-\frac{E_{an}}{k_b T_*}\right) \cdot \exp\left(-\frac{z_*}{z_0}\right) - x_{an,0} \frac{I_{short}}{C} \quad [28]$$

instead of solving Eq. 21, where T_* is the local temperature for the core, middle and surface layer.

Gas evolution model.—Previous studies have assumed the main component of SEI is $(CH_2OCO_2Li)_2$.[1] They showed the SEI decomposition reaction mechanism, which will release CO_2.[1,26]

$$(CH_2OCO_2Li)_2 \rightarrow Li_2CO_3 + C_2H_4 + CO_2 + 0.5O_2$$

Experiments on commercial 18650 Li-ion batteries from Lammer et al.[16] showed that during the first venting, most of the gas is CO_2. Based on these results, we assume that CO_2 is the main component of vented gas and it causes the gas pressure buildup process inside the cell before venting. Our study only models the initial gas generation of CO_2 coming from SEI decomposition which is important for early indication of a potential thermal runaway. The quantity of SEI consumed in mol can be expressed as:

$$n_{(CH_2OCO_2Li)_2} = \frac{\sum_* m_{an,*}(x_{SEI,0} - x_{SEI,*})}{2M_{C_6}} \quad [29]$$

where M_{C_6} is the mass per mol (g/mol) for C_6, the main component of anode when completed delithiated, and $n_{(CH_2OCO_2Li)_2}$ is the quantity of lithium-containing metastable species in SEI consumed in the reaction in mol. Since the SEI decomposition reaction mechanism shows the proportional constant for generated CO_2 and the consumed SEI quantity is 1, then the quantity of gas generated in mol can be expressed as:

$$n_{CO_2} = n_{(CH_2OCO_2Li)_2} = \frac{\sum_* m_{an,*}(x_{SEI,0} - x_{SEI,*})}{2M_{C_6}} \quad [30]$$

Hence the thermal model can be used to predict the gas pressure using the ideal gas law. As n_{CO_2} is a small number, for convenience, n_{CO_2} will be shown in mmol units in the following discussions.

The gas evolution model can be used to predict battery force changes during the early stage of a thermal runaway if the volume is known. During the early stages of TR, the cell's mechanical behavior is mainly due to the increased internal gas pressure within the cell. The force and gas pressure have different units, but the gas pressure can be used to predict the overall trend of cell mechanical behavior.

Table I. Pouch Cell Specification.

Cell Specification	Value
Anode Thickness (Double Sided with Current Collector)	$125\mu m$
Cathode Thickness (Double Sided with Current Collector)	$135\mu m$
Current Collector Thickness Anode	$13\mu m$
Current Collector Thickness Cathode	$13\mu m$
Separator Material	PE
Separator Porosity	40%
Separator Thickness	$12\mu m$
Anode Active Material Mass Fraction (Graphite:PVDF)	95:5
Cathode Active Material Mass Fraction (NMC111:CB:PVDF)	94:3:3
Electrode Active Material Loading (Anode Single Side)	$8.55 g/cm^2$
Electrode Active Material Loading (Cathode Single Side)	$18.5 g/cm^2$
Number of Double Sided Electrode Sheets Anode	15
Number of Double Sided Electrode Sheets Cathode	14
Electrolyte	1M $LiPF_6$
Organic Solvent in Electrolyte	2% EC:EMC (3:7)

Experimental

The batteries used in this experiment were manufactured at the University of Michigan Battery Lab. The pouch cell size is 133 $mm \times 89\ mm \times 4\ mm$. As shown in Figure 5a, a thermal runaway experiment using a 4.5 Ah Nickel Manganese Cobalt Oxide (NMC) pouch cell was set up to validate the model. The pouch cell was assembled with a hole in the separator covered by wax in one of the outer layers of the cell, the hole size is around 10 mm radius. The 1 kHz impedance of cell, from EIS testing, was 4.76 $m\Omega$ at 20°C. The experiment was performed for two pouch cells, one with 50% SOC and the other cell was fully charged (100% SOC). The battery specifications are provided in Table I.

The instrumented cell fixture was slowly heated in an Accelerating Rate Calorimeter (ARC) until the wax melted at around 57°C, and triggering an internal short circuit. The ambient temperature was measured with a T-type thermocouple. The thermocouple was placed between the current collecting tabs, and the reading was 63°C before the thermal runaway event. The whole ARC chamber was continuously heated at around 0.7°C/min and reached 63°C before the onset of the internal short circuit event. When the core part in the pouch cell reached its melting point (around 57°C) it triggered the ISC. A sketch of the sectional view of pouch cell tested is shown in Fig. 5b, to better illustrate the location and size of the initial ISC area.

The experiment measures battery surface temperature using an array with six thin film platinum RTD sensors,[27] as shown in Fig. 5a and Fig. 5b. At the same time, force is measured on the fixture using four load washers attached to the four corners of the fixture. The force signal is used to measure the expansion of the battery against the fixture. The peak force measured exceeds 400 pounds and is the result of gas pressure that built up inside the pouch during thermal runaway before cell venting. The ISC location and sensor locations are shown in Figure 5a and Figure 5b. Further details of the experiment and the tested battery cell are in Pannala's work[17] and Table I.

Results and Analysis

The model is compared with the two internal short circuit test results — Test One for the 100% SOC cell, Test Two for the 50% SOC cell. The cell with 50% SOC didn't go to thermal runaway, and instead

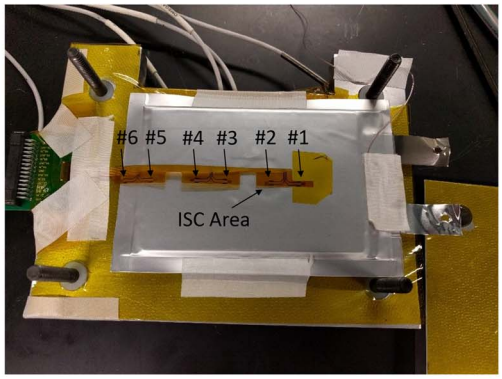

(a)

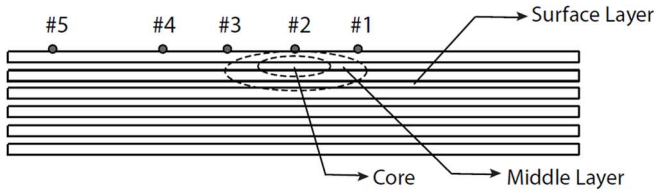

(b)

(c)

Figure 5. Experiment Setup (a) Cell Before Internal Short Test (b) Sensor Locations from Cross-Sectional View (c) Cell After Thermal Runaway.

experienced a slow self-discharge. The fully charged cell experienced a quick thermal runaway, as shown in Fig. 5c.

Before further discussing the experiment and comparing our model and the experimental results, a few assumptions have been made for the model. First, the relative volumes of the core and middle layer are tuned to match the experimental data. The core mass used for our simulation is chosen to be 1% of total mass to match the duration of the internal short circuit for 50% SOC cell. The middle layer is 4.5% of total battery mass based on a minimum least square error of the model and experimental surface temperature measured by sensor #5 in Fig. 5a.

The hole in the separator is around 10 mm in radius, and from previous discussion of ISC resistance, Eq. 12 can be used to estimate the short circuit resistance. The estimated R_{short} for this pouch cell is $3.68 m\Omega$. The melting point of Aluminum is 660°C, and around 1000°C for Copper, so the current collector will melt and at that point, the battery structure collapses. We can then assume that the internal short circuit will stop at sections with temperatures above 660°C. As the heat propagates to neighboring areas, an internal short starts in the neighboring areas after that collapse.

The equivalent thermal resistance can be calculated using cell heat conductivity ($\lambda_x = 21\ W/(m \cdot K)$, $\lambda_y = 21\ W/(m \cdot K)$,

Table II. Model Parameters.

Parameter	Value	Unit	Source	Physical Meaning
A_{an}	2.5×10^{13}	s^{-1}	[6, 22]	Frequency factor for anode decomposition
A_{ca}	2.55×10^{14}	s^{-1}	[22]	Frequency factor for cathode decomposition
A_{SEI}	2.25×10^{15}	s^{-1}	[22]	Frequency factor for SEI decomposition
A_{c2m}	628	mm^2	Approximated	Contact area for core to middle layer
A_{m2s}	1711	mm^2	Approximated	Contact area for middle layer to surface
C	4.5	Ah	Measured	Capacity of the Battery
C_p	1100	$J\,kg^{-1}K^{-1}$	[9]	Specific heat capacity of battery core
$C_{p,Al}$	897	$J\,kg^{-1}K^{-1}$	Approximated	Specific heat capacity of aluminum fixture
Δd_{c2m}	1	mm	Approximated	Core to middle layer mass center vertical distance
Δd_{m2s}	1.38	mm	Approximated	Middle layer to surface mass center vertical distance
E_{an}	2.24×10^{-19}	J	[6, 22]	Activation energy for anode decomposition
E_{ca}	2.64×10^{-19}	J	[22]	Activation energy for cathode decomposition
E_{SEI}	2.24×10^{-19}	J	[6, 22]	Activation energy for SEI decomposition
h_{an}	1714	$J\,g^{-1}$	[6, 22]	Enthalpy of anode decomposition
h_{ca}	790	$J\,g^{-1}$	[22]	Enthalpy of cathode decomposition
h_{SEI}	257	$J\,g^{-1}$	[6, 22]	Enthalpy of SEI decomposition
m_{an}	19.107	g	Measured	Mass of anode
m_{ca}	36.56	g	Measured	Mass of cathode
m_{cell}	103.75	g	Measured	Total mass of cell
m_{core}	1.038	g	Fitted	Mass of battery core
m_{fix}	1100	g	Measured	Mass of Aluminum fixture
m_{mid}	4.67	g	Fitted	Mass of battery middle layer
m_{surf}	98.04	g	Estimated∗	Mass of battery surface layer
r_{c2m}	3.18	$K \cdot W^{-1}$	Estimated∗	Thermal resistance between core and middle layer
r_{m2s}	1.61	$K \cdot W^{-1}$	Estimated∗	Thermal resistance between middle layer and surface
r_{s2a}	1.00	$K \cdot W^{-1}$	Estimated	Thermal resistance between surface layer and fixture
r_{fix}	1.73	$K \cdot W^{-1}$	Estimated	Thermal resistance between fixture and ambient air
R_{1kHz}	4.76	$m\Omega$	Measured	1 kHz cell impedance at 20°C
$R_{e,ref}$	0.0246	$m\Omega$	Approximated	Reference electrical resistance
R_{short}	3.68	$m\Omega$	Estimated∗	Short circuit resistance
SOC_0	1	-	Approximated	Initial State of Charge
T_{amb}	63	°C	Measured	Ambient temperature
T_{ref}	1543	K	[21]	Reference temperature
$x_{an,0}$	0.75	-	[6, 22]	Initial fraction of Li in anode for fully charged cells
$x_{SEI,0}$	0.15	-	[6, 22]	Initial fraction of Li in SEI
z_0	0.033	-	[6, 22]	Initial dimensionless SEI thickness
α_0	0.04	-	[6, 22]	Initial degree of conversion of cathode decomposition

∗Thermal resistance r_{c2m}, r_{m2s} are estimated by Eq. 31.
∗R_{short} is estimated by Eq. 12.
∗m_{surf} is estimated by conservation of mass ($m_{core} + m_{mid} + m_{surf} = m_{cell}$).

$\lambda_z = 0.5\ W/(m \cdot K)$[9]) and geometry of the three regions. As the shape of the pouch cell is long and flat, the thermal resistance in x and y direction is large. So we can approximate the thermal resistance by using the thermal resistance in z direction:

$$r_i = \frac{\Delta d_i}{\lambda_z A_i} (i = c2m, m2s) \quad [31]$$

where r_i is the thermal resistance for core to middle, or middle to surface, Δd_i is the vertical distance between the mass center of the core to middle layer, or the middle layer to surface layer, and A_i is the contact area in the x and y plane for core to middle, or middle to surface layer. In calculating thermal resistance, we assume the core and middle layer to be cylinders, with core layer cylinders at the center of the middle layer. For the core, as the ISC radius is 10 mm radius, and the core volume ratio is 1% from tuning result, We can then assume it as a cylinder with 10 mm radius and 1.51 mm height, which will correspond to 1% core volume ratio. For the middle layer, we assume its radius and height are proportional to the dimensions of the core and scaled by the 4.5% volume ratio, so it is a cylinder with 16.5 mm radius and 2.5 mm height. To be noticed, for the core and middle layer cylinders, the radius is much longer than the height, which satisfies the condition of using Eq. 31. If a case for small radius ISC is studied, and the cylinder radius and height are similar, then the thermal resistance on x and y direction needs to be considered. Although some assumptions are made in calculating thermal resistances, parametric study results show that multiplying or dividing the thermal resistances r_{c2m} and r_{m2s} by 10 won't significantly change the model results, which shows that the assumptions made here have limited impact on the model results. Based on these, Δd_i and A_i will be calculated and provided in Table II that are used to calculate r_{c2m} and r_{m2s}.

In addition, the experiment setup contains a compliant rubber foam pad and an aluminum fixture, which should be considered in the model to accurately represent the heat transfer to the ambient environment. The equivalent thermal resistance r_{s2a} now represents the thermal resistance between the battery surface and the aluminum fixture, so that the T_{amb} term in Eq. 3 will now be T_{fix}. The aluminum fixture is not an ideal heat sink, in this case, the temperature rise of the fixture can be expressed as:

$$C_{p,Al} \cdot m_{fix} \frac{dT_{fix}}{dt} = \frac{T_{surf} - T_{fix}}{r_{s2a}} + \frac{T_{amb} - T_{fix}}{r_{fix}} \quad [32]$$

where thermal resistance terms r_{s2a} and r_{fix} are correlated with the rubber foam properties and heat transfer process from air to fixture. For convenience, these two thermal resistance terms will be given in

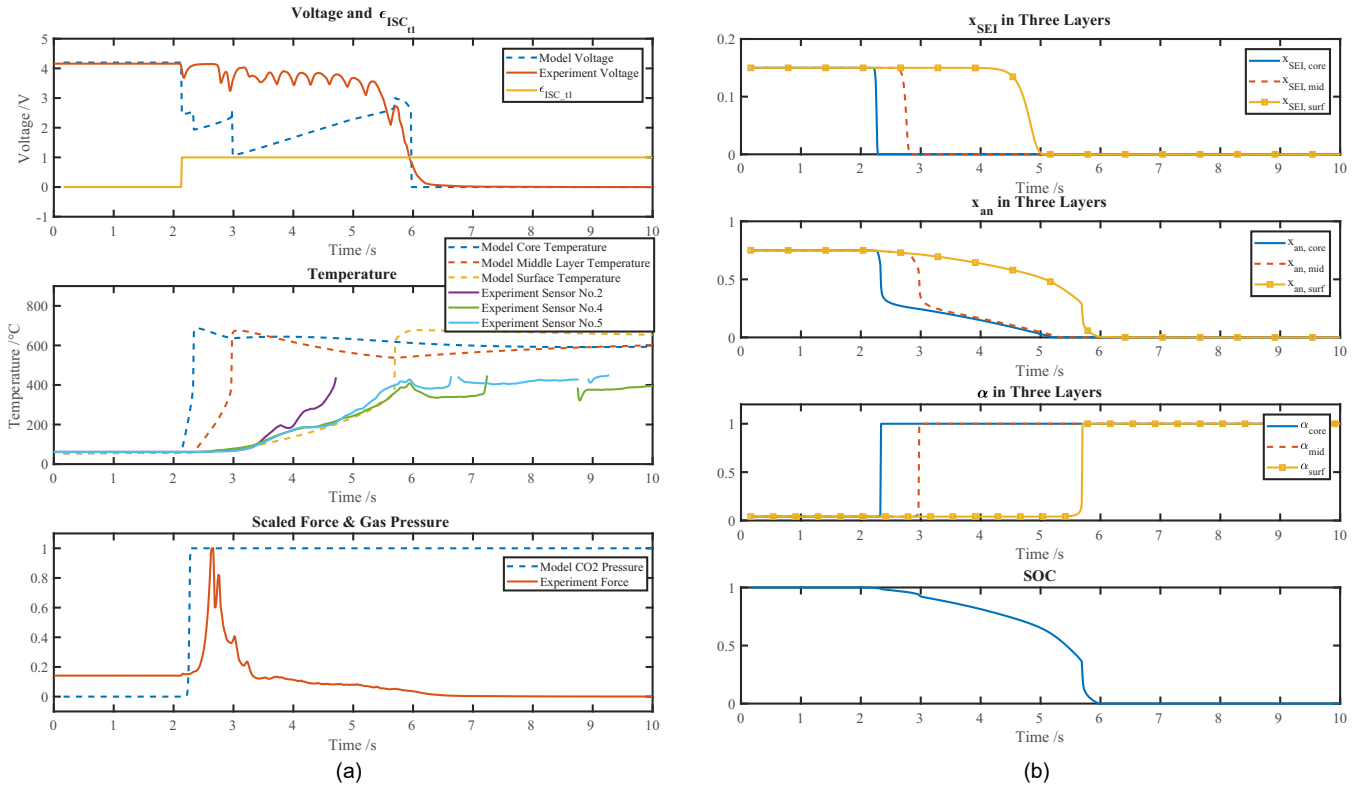

Figure 6. Test One Result (Catastrophic Thermal Runaway). (a) The Timings of the Voltage Drop and Temperature Rise with Battery Internal Pressure Build-up are Well Captured by the Model (b) Side Reaction Parameters Show the Side Reactions Sequence During a Thermal Runaway.

Table II directly. Other model parameters for the fully charged cell are also presented in Table II. The parameters come from existing literature, direct measurement, fitting, or an estimation based on the equations in this paper. The comparison between experiment result and model result for both tests will be shown in the following.

Test one: fully charged cell.—The first experiment was performed with a cell at 100% SOC, and it resulted in a thermal runaway. The behavior of fast voltage drop without recovering is referred to as Mode B in previous studies,[28] except in this case a quick thermal runaway event was triggered. As described by Feng,[1] the shrinkage and collapse of the separator following the shutdown caused a massive ISC, triggering a quick thermal runaway in the tested battery cell. The model assumes that for the fully charged cell, the propagation of ohmic heat leads to additional short-circuit regions after the initial short circuit area burns out.[28]

A function ϵ_{ISC_t1} is implemented here to control the state of ISC of Test One. $\epsilon_{ISC\_t1} = 0$ represents no massive ISC, while $\epsilon_{ISC\_t1} = 1$ represents an ongoing ISC in the cell.ϵ_{ISC_t1} is a function of maximum core temperature recorded in the model before time t_0, defined as $T_{max} = max\{T_{core}|_{t \le t_0}\}$, and can be expressed as:

$$\epsilon_{ISC\_t1} = \begin{cases} 1, & \text{if } T_{max} > 57^{\circ}C. \\ 0, & \text{otherwise.} \end{cases} \quad [33]$$

The Test One result is shown in Fig. 6a. The solid line shows the experimental result, and the dashed line is the model result. The side reaction parameters and SOC predicted by the model are shown in Fig. 6b.

Voltage analysis.—The voltage drop at t = 2.1s in Fig. 6a represents the start of the internal short circuit event. When the voltage drops to zero, the ohmic heat generation stops. The oscillation in the measured voltage is the result of the intermittent connection of the ISC due to structural changes at high temperature. The model predicts a stepwise voltage drop because we assume the ISC area will expand to the neighboring area, and as discussed above, the larger ISC area will decrease the R_{short}, and decrease the terminal voltage. The model voltage increases at 3 to 5 seconds and this is due to R_{cell} decrease with temperature rise, while the R_{short} stays constant with temperature change.

To be noticed, voltage is also a function of SOC. However, the SOC-voltage curve is relatively flat, as seen in 2b. The influence of the SOC change in voltage is relatively small in this thermal runaway event. On the overall time scale, the model matches with experiment data and captures the total battery failure time with the experiment.

Temperature analysis.—The RTD sensors are located in different regions of the pouch cell, as seen in Figure 5a. The ISC trigger device is located near the surface, as described by Pannala.[17] As seen from the sensor locations of Fig 5b, the RTD sensor #2 corresponds to the surface layer in the model but is physically located directly above the ISC area. RTD sensor #1, #3 and #4 measure the temperatures at the surface, each RTD sensor is spaced 1.75 mm apart,[27] RTD sensor #5 measures the temperature of the bulk surface.

The second subplot in Figure 6a shows the comparison of model and experimental temperatures. The experimental data above 450°C has been ignored, because the melting point of Kapton used in RTD sensor is 400°C. The readings from RTD sensor #1 and #2 are very similar due to their close proximity, the same for RTD sensor #3 and #4. RTD sensor #6 was damaged prior to installation, and could not be used. For readability, only data from sensor #2, #4 and #5 will be presented and analyzed.

The RTD sensor #2 is at the surface layer of the battery model, but it is located above the middle layer and core part, so its response should be close to our modeled middle layer temperatures. The experimental data from RTD sensor #2 (the purple solid line in the plot) is in between the modeled middle layer temperature (dashed red line) and the modeled surface temperature (dashed yellow line), and this is due

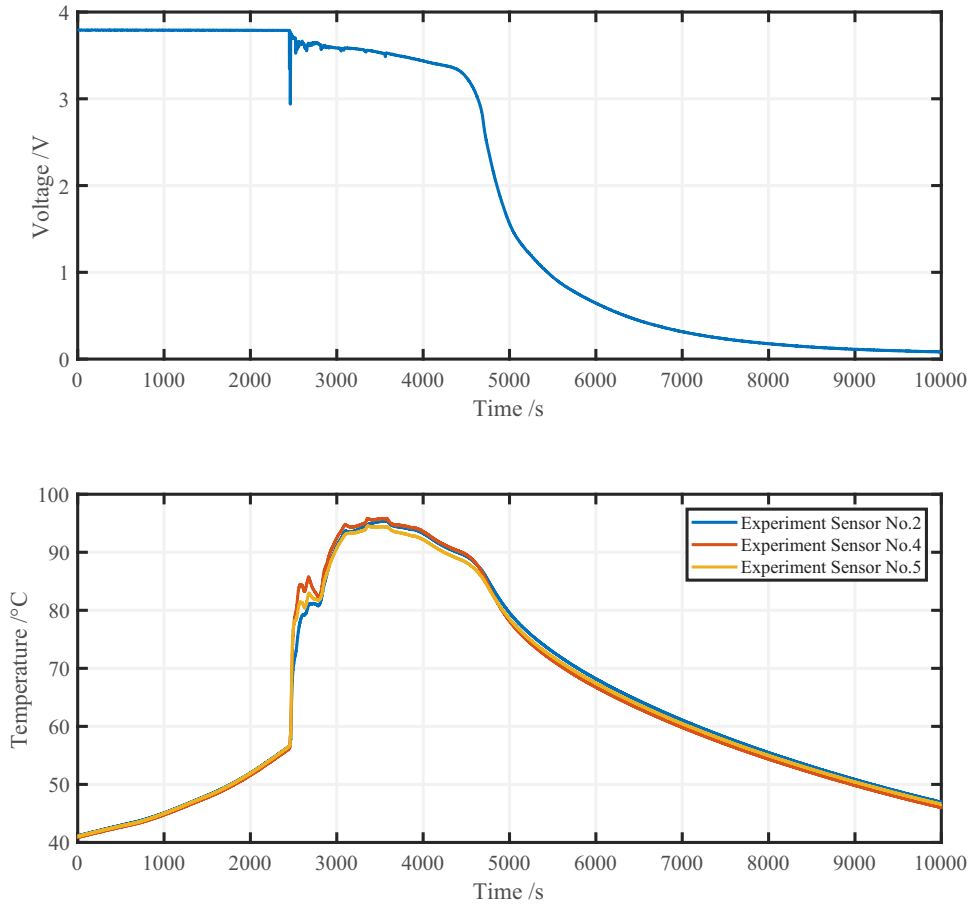

Figure 7. Test Two Result (Slow Self-discharge), Showed the Terminal Voltage and Temperature Profile of the 50% SOC Cell over 10000 seconds. No Thermal Runaway was Observed, but a Slow Self-discharge Process After Triggering ISC.

to the small middle layer chosen in this study, so the RTD sensor #2 response will be slower than the modeled middle layer temperature. RTD sensor #4 (green solid line) and #5 (blue solid line) measure the surface temperature and match well with the modeled surface layer temperature.

The model matches well with the temperature measured experimentally, which indicates that this pouch cell can be modeled using the proposed three-section model. However, a highly discretized distributed model or 3D finite element method is recommended if the temperature at different points of the cell surface is the main focus.

At around 5.8 seconds, the model shows a sudden surface temperature rise. This sudden rise is due to cathode decomposition in the surface layer which released a vast amount of energy in a short time around 5.8 seconds, as shown in Fig. 6b. The sudden rise of surface temperature also increased other exothermic reactions including anode decomposition, which depleted SOC in the cell. At 5.8 seconds, the cell reached peak surface temperature, and it completed the exothermic reactions and internal short circuit process in this thermal runaway event.

Force & gas analysis.—As there is no good way of measuring battery core temperature directly in the experiment, the force measurement is the chosen alternative for early detection of thermal runaway inside the battery.

From the experimental data, we see a sharp rise and drop of force measurement. Compared with the battery force signal at the start of the experiment, the force increased 2.5 pounds due to battery thermal expansion caused by a 30°C temperature increase. After the short circuit, before venting, the peak force rose over 400 pounds. The sharp rise of force is the result of pressure that is built up due to formed gas. Pannala[17] using a thermocouple placed between the tabs also detected vented hot gases following a quick drop of force. So the quick drop of force is the result of venting of the pouch.

In the model, the primary source of CO_2 during the early stage of thermal runaway is assumed to come from SEI breakdown. The model force comes from gas pressure buildup due to SEI breakdown in the core section.

According to the observed decomposition reactions of each layer in the three-section model, the predicted gas generation will include additive contributions from each of three sections, core, middle layer, and surface layer. A significant amount of gas is generated when the middle layer and surface layer reach the critical temperature. However, since the pouch breaks soon after the first stage gas pressure buildup, only the CO_2 generated in core section is presented in the third subplot of Fig. 6a. Also, since the force measurement and gas pressure have different scale units, so the force data and gas pressure are both normalized to 1 using the maximum value over the experiment duration.

From the third subplot of Fig. 6a, the two peaks of force and predicted gas pressure aligns well. The model successfully captures the battery core temperature rise prior to surface temperature rise, and the timing of core temperature rise matches well with our experimental force measurement. The model is able to capture the feature of gas pressure buildup during a fast internal short circuit event.

Test two with 50% SOC cell.—For the cell with 50% SOC, that was also heated to 57°C, an ISC was triggered but didn't evolve into a catastrophic thermal runaway. In Test Two, the cell experienced a rapid decrease and subsequent recovery of voltage after the ISC was triggered. It then progressed to a slow self-discharge process that

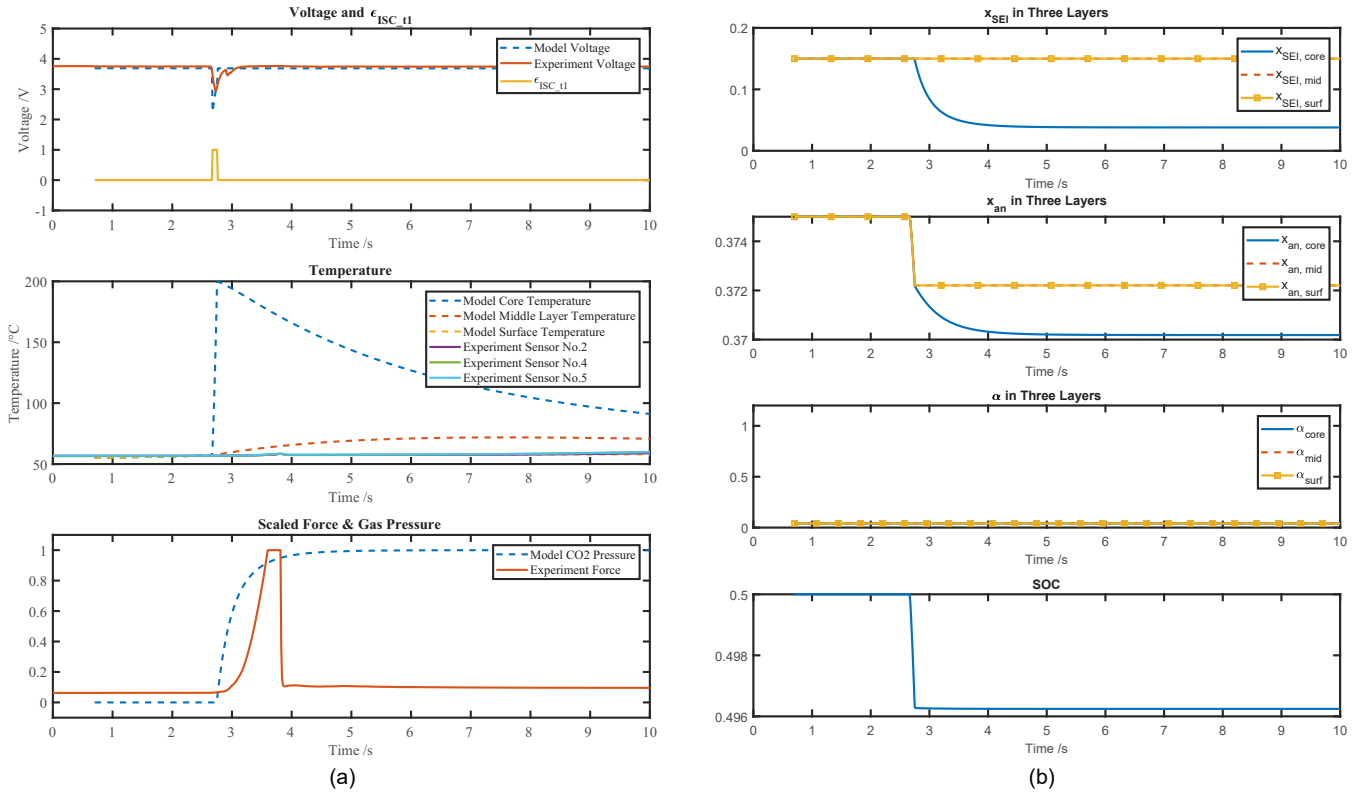

Figure 8. Test Two Result (Slow Self-discharge). (a) The Model Matches the Measured Voltage, Temperature, and Build-up of Internal Pressure Well (b) Side Reaction Parameters Show the SEI Decomposition Is the Only Active Side Reaction.

completely used up the available lithium ions after 8000 seconds. Fig. 7 shows this behavior in our experiment over 10000 seconds. This behavior is similar to the result in a previous study on internal short-circuit, described as Mode A[28] or fusing phenomenon.[29] In the fusing phenomenon, the shutdown of the internal short circuit and the quick voltage recovery happen because of the burnt-out of the area around the initial ISC. Then a following small-scale ISC event occurs resulting in a slow self-discharge process.[29]

Kim[28] used an infrared camera and showed the peak temperature for the nail penetration region in a Mode A short is around 200°C to 210°C. In the current model, 200°C will be used as the critical temperature of Mode A. The ISC stops after the core region reaches 200°C. This temperature range fits well with both experimental and model data in this study.

For Test Two, the internal short circuit was assumed to shut down when the core temperature reached 200°C. Similar to Test One, a function ϵ_{ISC_t2} is implemented here to control the state of ISC of Test Two. $\epsilon_{ISC\_t2} = 0$ represents no massive ISC, while $\epsilon_{ISC\_t2} = 1$ represents an ongoing ISC in the cell. Defined same as test one, $T_{max} = max\{T_{core}|_{t \le t_0}\}$. ϵ_{ISC_t2} is a function of T_{max}, and can be expressed as:

$$\epsilon_{ISC\_t2} = \begin{cases} 1, & \text{if } T_{max} > 57°C \ \& \ T_{max} \le 200°C. \\ 0, & \text{otherwise.} \end{cases} \quad [34]$$

Test Two result is shown in Fig. 8a. The solid line represents the experiment results, and the dashed line is the model prediction. The side reaction parameters predicted by the model are given in Fig. 8b.

Voltage analysis.—The first subplot of Fig. 8a is a comparison of voltage from the experiment and model. The voltage drop at t = 2.65 s represents the start of the internal short circuit event. The model matches with experimental data on the timescale and overall trend. It also successfully shows the interruption of the ISC and the voltage recovers to its nominal working range.

Temperature analysis.—Temperature sensor locations for Test Two are the same for Test One. In this test, the cell didn't trigger a quick thermal runaway.

As the core temperature reached 200°C, the ISC stopped due to burn-out of the short circuit region, so the ISC process only lasted for a small period of time and caused core layer temperature rise only. RTD sensors located on the battery surface showed few changes in their readings during the ISC process. The model prediction matches well with the middle layer and surface layer temperature, and at the same time predicts core temperature rise (blue dashed line), which cannot be measured by RTD sensors in the experiment.

Force & gas analysis.—Similar to Test One, force measurements can be used to detect potential ISC within the cell. From the third subplot of Fig. 8a for Test Two, the time for the peak of force and the rising time for gas pressure align well. The model captures the battery core temperature rise, and while at the same time shows that the battery didn't progress into a quick thermal runaway.

Analysis for different ISC modes.—Both Test One and Test Two were conducted under the same conditions, except for cell SOC but each progressed to a different ISC event. The fully charged cell went into thermal runaway while the 50% SOC cell experienced fusing phenomenon and didn't explode. However, SOC is not the only factor in determining the ISC mode. Previous nail penetration experiments and computational analysis pointed out that SOC, separator material[28] and ISC radius[29] will all affect the types of ISC mode.

It is possible that the temperature increase speed for core and neighboring layers is the dominant factor for ISC mode. Unlike the fully charged cell, the 50% SOC cell had a slower temperature rise and a smaller spatial temperature gradient, which in the end didn't trigger a massive additional short circuit that can lead to a catastrophic thermal runaway.

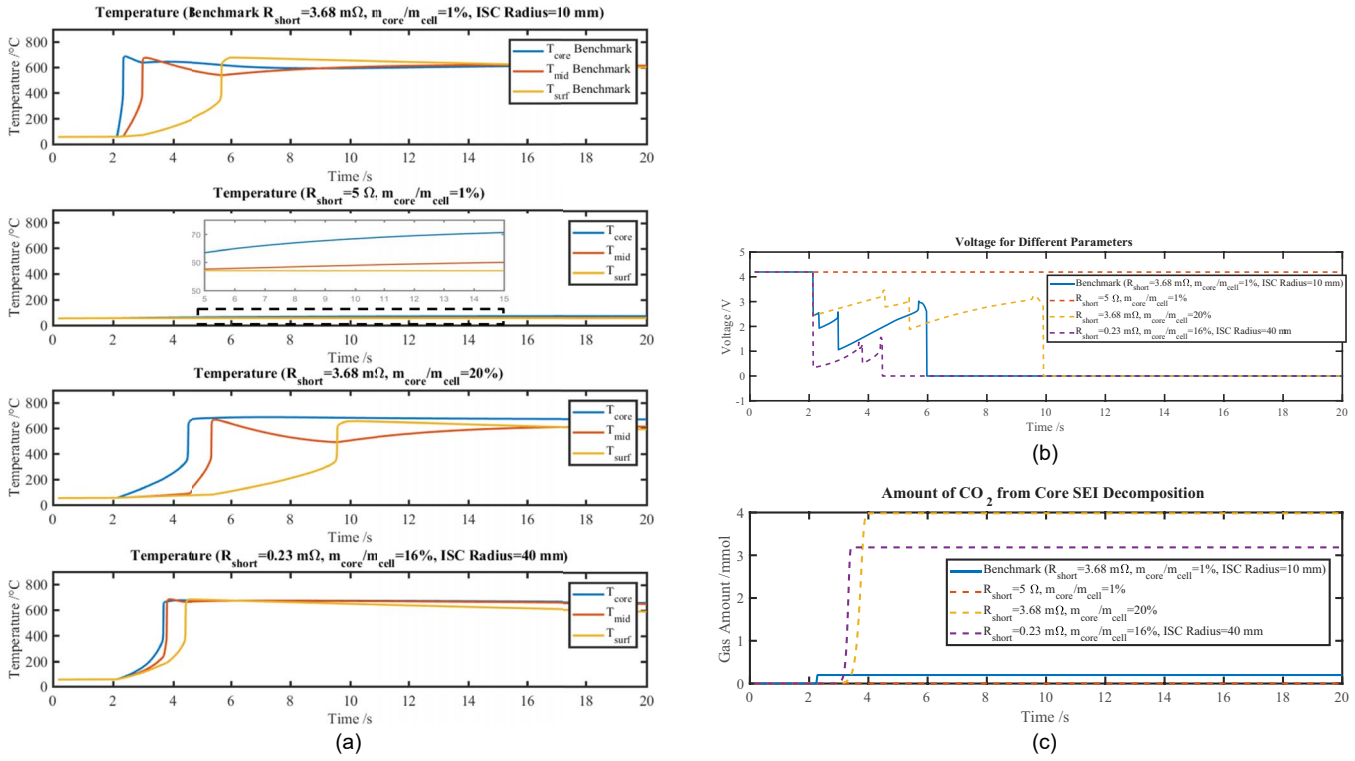

Figure 9. Model Parametric Study on ISC Resistance, Core Mass Ratio and ISC Radius. (a) Temperature, (b) Voltage, (c) CO_2 Generation by SEI Decomposition in Core Area.

In this study, different model settings of ISC modes are given for Test one and Test two to describe the results. However, future work with more internal short circuit tests is required to study the criteria to predict whether the cell triggers thermal runaway or not during an ISC event.

Model Parametric Study

Most of the parameters in the proposed model come from the battery's physical properties. In this study, with the ISC area known, parameters like ISC resistance can be estimated. However, when applying this model to a real case, the ISC resistance and ratio of core mass to total cell mass are usually unknown and need to be tuned to match the experimental data. A parametric study of the thermal runaway model will help to explore the sensitivity of parameters on the model. In this parametric study, ISC resistance, core mass ratio and ISC radius will be studied.

For a parametric study of ISC radius, anode to cathode ISC will be the focus, as an anode to cathode ISC is the most common type of ISC.[18] In such a case, changes made to the ISC radius will be applied to both ISC resistance and core mass ratio. As discussed in previous sections, ISC resistance is a function of ISC radius, and the increase of ISC radius will decrease ISC resistance as a result of the larger ISC area. The core mass ratio is also a function of the ISC radius. The core section is the battery area affected by the initial ISC, and as expressed by Eq. 4: $V_{core} = \pi r_{short}^2 H$, where r_{short} is the radius of short, and H is the height of the cylindrical short area. The increase of ISC radius will increase the core mass. The parameters used in experimental sessions will serve as a benchmark case for our model parametric study, with ISC resistance 3.68 $m\Omega$, core mass ratio 1%, and ISC radius of 10 mm.

ISC resistance.—In this section, ISC resistance will be changed to study the influence of model parameters on the prediction of the electrical, thermal and mechanical behavior. Feng[9] used $R_{short} = 20\ \Omega$ to study the online detection of ISC. For comparison, ISC resistance will be chosen 5 Ω in this parametric study, while the benchmark ISC resistance is 3.68 $m\Omega$.

The second subplot for Fig. 9a and red dashed line in Fig. 9b shows the temperature and voltage predicted by the model given different ISC resistances. From the plot, we see the temperature rise of a cell with low ISC resistance is much quicker and depletes its active material in less than 10 seconds. The cell with high ISC resistance releases the heat slowly, and won't trigger a thermal runaway event. Increasing the resistance will slow the ISC process and possibly prevent a potential thermal runaway event.

Large ISC resistance will have a slow temperature rise, and usually represents micro-shorts in the battery or separator penetrated by a low electric conductivity material. The parametric study of this model can be used to predict the severity of an ISC event, and based on its short circuit radius, it may predict whether the cell will trigger thermal runaway or not.

Fig. 9c shows the amount of CO_2 generated by core SEI decomposition. With ISC resistance so large, the core area will not reach its SEI decomposition critical temperature, even after a few minutes. In this case, the amount of gas generated is limited and can hardly be detected by force or gas sensors.

Core mass ratio.—In this section, we demonstrate the effect of changing the core layer mass ratio. The core layer mass ratio is chosen to be 20% of total cell mass, while the benchmark core mass ratio is 1%.

The third subplot for Fig. 9a and yellow dashed line in Fig. 9b shows the temperature and voltage predicted by the model given different core mass ratios. From the plot, we see that with high core mass ratio, the time to reach thermal runaway has been delayed. This is due to the increased effective thermal mass of the core area which decreases the rate of temperature rise and delays the time at which a critical temperature for exothermic reactions is achieved.

Cathode to anode ISC with different ISC radius.—Previous parametric studies have revealed the influence of critical ISC parameters on model performance. For the most common Cathode to Anode ISC, with high conductivity material crossing the separator, core mass ratio and ISC resistance are both a function of ISC area, as indicated by Eq. 4 and Eq. 12. Changes in ISC area will influence the ISC resistance and core mass ratio.

In this study, the ISC radius is chosen as 40 mm, while the benchmark is 10 mm. From the previous discussion of Thermal runaway model section, for ISC radius of 10mm and 40mm, the geometric resistance (R_{geo}) is sufficient for calculation. The resulting electric resistances are 3.68 $m\Omega$ and 0.23 $m\Omega$, respectively. The core mass ratio for our benchmark is 1%, and with the ISC radius increase to 40 mm, the core mass ratio will now increase from 1% to 16%. The increased mass ratio reflects the increased ISC area. The thermal resistance term r_{c2m} also changes accordingly with the change of contact area for the core to middle layer by Eq. 31. The simulation results with the different ISC radius are presented in the fourth subplot of Fig. 9a and Fig. 9b.

From the plot, we see that for Cathode to Anode ISC, at large ISC radius, the temperature distribution in the battery is more uniform. The difference between the three temperature states is small throughout the whole process of thermal runaway. A large ISC radius will make the ISC process seem to approach an external short circuit process. In this specific condition, the three-state thermal model predicts similar temperature dynamics as a lumped thermal model, and a lumped model would be accurate enough.

Conclusions

A model for Li-ion battery thermal runaway has been formulated using a three section discretization. The three sections correspond to three battery temperature states: the core temperature, middle layer temperature, and surface layer temperature. A side reaction model, an electrical model, a gas evolution model are also developed and integrated in a unified framework. The model matches well with the experiment results after parameter tuning. Especially, the predicted gas pressure from the gas evolution model matches well with battery force during the early stage of thermal runaway. This force behavior indicates a potential method for the early detection of thermal runaway.

In the experiment, an internal short circuit is triggered at the core part of two pouch cells. Test One cell with 100% SOC triggered quick thermal runaway, while the other test cell, with 50% SOC, didn't go to thermal runaway. The model captures the voltage, temperature, and force well for both cases when given the type of ISC mode. The three-section model can describe both an ISC induced thermal runaway event, as well as an event where the hard short was interrupted leading to gradual self-discharge without sufficient temperature rise to trigger TR.

The significant difference between our two tests is whether the ISC shuts down or leads to additional ISC after the burn-out of the initial ISC. This difference leads to two different results, a catastrophic thermal runaway or a safe, slow self-discharge process. Future work including more internal short circuit experiments is needed to study the criteria that differentiate such cases. The model now has three adjustable parameters (m_{core}, m_{mid}, ϵ_{ISC}). With future work on ISC mode criteria, we can reduce the tuned parameters to two (m_{core}, m_{mid}). With more experiments to validate the model, we will enable the full predictive capability of this low order three section model.

We have demonstrated experimentally that force measurement can be useful for describing the initial stages of an ISC event regardless of whether or not thermal runaway follows. Combined with a three-section thermal model describing the chemical reactions of material break down, this measurement can be used for diagnosing ISC or thermal runaway events faster and with higher confidence levels than voltage and temperature sensing alone.

Acknowledgment

This material is based upon work supported by the National Science Foundation under Grant No. 1762247, and was supported in part by Battery Solutions Inc and the State of Michigan through the Small Company Innovation Program (SCIP). The authors wish to acknowledge the technical and financial support of the Automotive Research Center (ARC) in accordance with Cooperative Agreement W56HZV-14-2-0001 U.S. Army Tank Automotive Research, Development and Engineering Center (TARDEC) Warren, MI. The authors wish to acknowledge Greg Less and the University of Michigan Battery Lab for providing the battery cells, assisting in embedding the wax-based separator, and the guiding through the use of Accelerated Rate Calorimeter. The authors wish to acknowledge Aaron Knobloch from General Electric for providing the temperature sensors under the ARPA-E AMPED program. The authors would like to thank Mingxuan Zhang for embedding the wax-based ISC device, Sravan Pannala for collecting and analyzing the experimental data and Suhak Lee for assisting in EIS testing.

List of Symbols

A_{an}	Frequency factor for anode decomposition, s^{-1}
A_{ca}	Frequency factor for cathode decomposition, s^{-1}
A_{SEI}	Frequency factor for SEI decomposition, s^{-1}
C	Capacity of the Battery, Ah
C_p	Specific heat capacity of battery core, $Jkg^{-1}K^{-1}$
$C_{p,Al}$	Specific heat capacity of aluminum, $J \cdot kg^{-1} \cdot K^{-1}$
E_{an}	Activation energy for anode decomposition, J
E_{ca}	Activation energy for cathode decomposition, J
E_{SEI}	Activation energy for SEI decomposition, J
h_a	Enthalpy of anode decomposition, $J \cdot g^{-1}$
h_c	Enthalpy of cathode decomposition, $J \cdot g^{-1}$
h_s	Enthalpy of SEI decomposition, $J \cdot g^{-1}$
I_{short}	Short circuit current, A
k_b	Boltzmann constant, $J \cdot K^{-1}$
k_r	ISC resistance temperature coefficient, K
m_{an}	Mass of anode, g
m_{ca}	Mass of cathode, g
m_{cell}	Total mass of cell, g
m_*	Mass of battery layer *, g
m_{fix}	Mass of aluminum fixture, g
$\dot{Q}_{an}$	Heat rate of anode decomposition, W
$\dot{Q}_{ca}$	Heat rate of cathode decomposition, W
$\dot{Q}_{SEI}$	Heat rate of SEI decomposition, W
$\dot{Q}_{exo,*}$	Heat rate of exothermic side reactions in layer *, W
$\dot{Q}_{ohmic,*}$	Heat rate of short circuit ohmic heat in layer *, W
r_{c2m}	Equivalent thermal resistance between battery core and middle layer, $K \cdot W^{-1}$
r_{m2s}	Equivalent thermal resistance between battery middle layer and surface layer, $K \cdot W^{-1}$
r_{s2a}	Equivalent thermal resistance between battery surface layer and ambient, $K \cdot W^{-1}$
r_{fix}	Equivalent thermal resistance between fixture and its ambient air, $K \cdot W^{-1}$
R_{cell}	Cell electrical resistance, Ω
R_{3D}	Electrical resistance calculated by 3D simulation, Ω
R_{geo}	Geometric electrical resistance, Ω
R_{short}	Short circuit resistance, Ω
SOC	State of Charge, -
SEI	Solid Electrolyte Interface, -
T_*	Temperature of battery layer *, $^\circ C$
T_{amb}	Ambient temperature, $^\circ C$
T_{fix}	Temperature of aluminum fixture, $^\circ C$

$U(SOC)$	Battery open circuit voltage vs SOC, V
$x_{an,*}$	Fraction of Li in anode in layer *, -
$x_{an,0}$	Initial fraction of Li in anode, -
$x_{SEI,*}$	Fraction of Li in SEI in layer *, -
$x_{SEI,0}$	Initial fraction of Li in SEI, -
z_*	Dimensionless SEI thickness in layer *, -
z_0	Initial dimensionless SEI thickness, -

Greek

α_*	Degree of conversion of cathode decomposition in layer *, -
α_0	Initial degree of conversion of cathode decomposition, -
ϵ_{ISC_t1}	State of internal short circuit of test one, -
ϵ_{ISC_t2}	State of internal short circuit of test two, -
ρ	Electrical resistivity, $\Omega \cdot$ m

Subscripts

$*_{core}$	core layer, -
$*_{mid}$	middle layer, -
$*_{surf}$	surface layer, -
$\#_{an}$	anode, -
$\#_{ca}$	cathode, -
$\#_{SEI}$	SEI, -

ORCID

Ting Cai https://orcid.org/0000-0001-8343-9032
Jason B. Siegel https://orcid.org/0000-0003-2824-013X

References

1. X. Feng, M. Ouyang, X. Liu, L. Lu, Y. Xia, and X. He, *Energy Storage Materials*, **10**, 246 (2018).
2. R. Spotnitz and J. Franklin, *J. Power Sources*, **113**, 81 (2003).
3. S. Abada, G. Marlair, A. Lecocq, M. Petit, V. Sauvant-Moynot, and F. Huet, *J. Power Sources*, **306**, 178 (2016).
4. T. Cai, A. Stefanopoulou, and J. Siegel, in *Dynamic Systems and Control Conference*, ASME: 2018.
5. T. D. Hatchard, D. D. MacNeil, A. Basu, and J. R. Dahn, *J. Electrochem. Soc.*, **148**, A755 (2001).
6. P. T. Coman, E. C. Darcy, C. T. Veje, and R. E. White, *J. Electrochem. Soc.*, **164**, A587 (2017).
7. C. Zhang, S. Santhanagopalan, M. A. Sprague, and A. A. Pesaran, *J. Power Sources*, **290**, 102 (2015).
8. G.-H. Kim, K. Smith, J. Ireland, and A. Pesaran, *J. Power Sources*, **210**, 243 (2012).
9. X. Feng, C. Weng, M. Ouyang, and J. Sun, *Appl. Energy*, **161**, 168 (2016).
10. R. Guo, L. Lu, M. Ouyang, and X. Feng, *Sci. Rep.*, **6** (2016).
11. M. N. Richard, *J. Electrochem. Soc.*, **146**, 2078 (1999).
12. G.-H. Kim, A. Pesaran, and R. Spotnitz, *J. Power Sources*, **170**, 476 (2007).
13. D. Ren, X. Liu, X. Feng, L. Lu, M. Ouyang, J. Li, and X. He, *Applied Energy*, **228**, 633 (2018).
14. T. Cai, A. G. Stefanopoulou, and J. B. Siegel, *Electrochemical Society Transactions*, **89**, 85 (2019).
15. P. T. Coman, S. Rayman, and R. E. White, *Journal of Power Sources*, **307**, 56 (2016).
16. M. Lammer, A. Königseder, and V. Hacker, *RSC Advances*, **7**, 24425 (2017).
17. S. Pannala, M. Zhang, J. Siegel, G. Less, and A. Stefanopoulou, in *ECS Meeting Abstracts*, Vol. MA2018-01 (3) 2151-2041 pp. 368–368 (2018).
18. M. Zhang, J. Du, L. Liu, A. Stefanopoulou, J. Siegel, L. Lu, X. He, X. Xie, and M. Ouyang, *J. Electrochem. Soc.*, **164**, A3038 (2017).
19. D. P. Finegan, E. Darcy, M. Keyser, B. Tjaden, T. M. Heenan, R. Jervis, J. J. Bailey, R. Malik, N. T. Vo, O. V. Magdysyuk et al., *Energy & Environmental Science*, **10**, 1377 (2017).
20. A. Rheinfeld, A. Noel, J. Wilhelm, A. Kriston, A. Pfrang, and A. Jossen, *Journal of The Electrochemical Society*, **165**, A3427 (2018).
21. S. Yang, B. Yan, J. Wu, L. Lu, and K. Zeng, *ACS applied materials & interfaces*, **9**, 13999 (2017).
22. X. Lin, H. E. Perez, J. B. Siegel, A. G. Stefanopoulou, Y. Li, R. D. Anderson, Y. Ding, and M. P. Castanier, *IEEE Transactions on Control Systems Technology*, **21**, 1745 (2013).
23. T. Dong, P. Peng, and F. Jiang, *Int. J. Heat Mass Transfer*, **117**, 261 (2018).
24. P. Ping, Q. Wang, P. Huang, J. Sun, and C. Chen, *Appl. Energy*, **129**, 261 (2014).
25. X. Feng, M. Fang, X. He, M. Ouyang, L. Lu, H. Wang, and M. Zhang, *J. Power Sources*, **255**, 294 (2014).
26. H. Yang, H. Bang, K. Amine, and J. Prakash, *Journal of the Electrochemical Society*, **152**, A73 (2005).
27. A. Knobloch, C. Kapusta, J. Karp, Y. Plotnikov, J. Siegel, and A. Stefanopoulou, *J. Electron. Packag.* (2018).
28. C.-S. Kim, J.-S. Yoo, K.-M. Jeong, K. Kim, and C.-W. Yi, *J. Power Sources*, **289**, 41 (2015).
29. M. Zhang, L. Liu, A. Stefanopoulou, J. Siegel, L. Lu, X. He, and M. Ouyang, *J. Electrochem. Soc.*, **164**, A2738 (2017).